The Sensitivity of WRF Daily Summertime Simulations over West Africa to Alternative Parameterizations. Part I: African Wave Circulation

ERIK NOBLE

University of Colorado Environmental Studies Program, Boulder, Colorado, and NASA Goddard Institute for Space Studies, New York, New York

LEONARD M. DRUYAN AND MATTHEW FULAKEZA

Columbia University Center for Climate Systems Research, New York, New York

ABSTRACT

The performance of the NCAR Weather Research and Forecasting Model (WRF) as a West African regional-atmospheric model is evaluated. The study tests the sensitivity of WRF-simulated vorticity maxima associated with African easterly waves to 64 combinations of alternative parameterizations in a series of simulations in September. In all, 104 simulations of 12-day duration during 11 consecutive years are examined. The 64 combinations combine WRF parameterizations of cumulus convection, radiation transfer, surface hydrology, and PBL physics. Simulated daily and mean circulation results are validated against NASA's Modern-Era Retrospective Analysis for Research and Applications (MERRA) and NCEP/Department of Energy Global Reanalysis 2. Precipitation is considered in a second part of this two-part paper. A wide range of 700-hPa vorticity validation scores demonstrates the influence of alternative parameterizations. The best WRF performers achieve correlations against reanalysis of 0.40–0.60 and realistic amplitudes of spatiotemporal variability for the 2006 focus year while a parallel-benchmark simulation by the NASA Regional Model-3 (RM3) achieves higher correlations, but less realistic spatiotemporal variability. The largest favorable impact on WRF-vorticity validation is achieved by selecting the Grell–Devenyi cumulus convection scheme, resulting in higher correlations against reanalysis than simulations using the Kain–Fritch convection. Other parameterizations have less-obvious impact, although WRF configurations incorporating one surface model and PBL scheme consistently performed poorly. A comparison of reanalysis circulation against two NASA radiosonde stations confirms that both reanalyses represent observations well enough to validate the WRF results. Validation statistics for optimized WRF configurations simulating the parallel period during 10 additional years are less favorable than for 2006.

1. Introduction

The National Center for Atmospheric Research (NCAR) developed the Weather Research and Forecasting Model (WRF) (Skamarock et al. 2008) to facilitate research into predominately midlatitude mesoscale and cloud-scale atmospheric phenomena. WRF is a community model whose use is not only rapidly expanding for operational and research NWP applications, but also for regional climate model (RCM) applications. An RCM is an NWP model nested within a general circulation model (GCM) or global-observation-based

dataset (reanalysis) that simulates atmospheric processes and soil hydrology while accounting for high-resolution topographical data, land–sea contrasts, surface characteristics, and other components of the earth system (Giorgi 1990). Since RCMs cover a limited domain, they require forcing data at their lateral boundaries as well as prescribed sea surface temperatures from a coarser GCM or reanalysis. RCMs can be initialized by the same datasets from which lateral boundary conditions are derived. RCMs thus downscale reanalysis or GCM scenarios to simulate climate variability with regional refinements (Giorgi and Mearns 1991). Published studies demonstrate WRF-RCM simulation skills for North America (Leung and Qian 2009; Bukovsky and Karoly 2011), Europe (Heikkilä et al. 2010), the Arctic (Cassano et al. 2011), and the Antarctic (Bromwich et al. 2013).

Crétat et al. (2012) test three cumulus convection physics schemes (CPSs), planetary boundary layer (PBL) and cloud microphysics schemes (MPSs) in WRF simulations over South Africa, running the model at 35-km horizontal grid spacing. They find that rainfall location and intensity are predominantly sensitive to convection, and much less to PBL and microphysics. The Kain–Fritsch (Kain 2004) and Grell–Dévényi (Grell 2002) CPSs tend to produce wet rainfall amount biases, while the reverse occurs for the Betts–Miller–Janjić (Janjić 2002) CPS. Pohl et al. (2011) test WRF skill over East Africa, including sensitivity to physical parameterizations of CPS, MPS, PBL, land surface model (LSM), and radiation schemes (RAD), as well as land-use categories. They find that the shortwave RAD and the LSM exert the largest influence on simulated rainfall, while the choice of CPS has a discernable but smaller influence. Less has been reported on testing the WRF-RCM performance for West Africa (WA), which is the focus of this study. Such tests of alternative WRF parameterizations by Flaounas et al. (2011) are described below.

West Africa includes a semiarid region known as the Sahel, located at 10°–20°N, between the Sahara Desert and the Gulf of Guinea coast. The West African monsoon (WAM) rainy season occurs during June–September, accounting for the single largest source of annual rainfall to the Sahel. The Sahel remains dry during the winter and spring months until rains arrive in late June from a northward inland surge of moist monsoon air from the Gulf of Guinea coast, marking the arrival of the WAM, suitably termed WAM onset (Sultan and Janicot 2000; Hagos and Cook 2007; Flaounas et al. 2011).

Although climate-model-based studies relate to monthly or seasonal mean fields, confidence in seasonal climate prediction improves if the model realistically captures the characteristics of relevant daily weather phenomena. Among the most significant relevant daily weather phenomena responsible for Sahel precipitation variability are mesoscale convective systems (MCSs), which are responsible for some 90% of annual rainfall (Lebel et al. 2003). MCSs are organized by African easterly waves (AEWs), summertime synoptic-scale atmospheric easterly waves that propagate westward from Sudan through West Africa and over the southeastern North Atlantic Ocean within the latitude range of 10°–20°N (Burpee 1972). AEWs have wavelengths of 3000–5000 km and periods of 3–5 days. Spectral analysis also detects a 6–9-day periodicity in easterly circulation, mostly over the northern Sahel (Diedhiou et al. 1999; Druyan et al. 2006). AEW generation can be attributed to the vertical and horizontal shear associated with the 700-hPa African easterly jet (AEJ), reflecting the combined influences of baroclinic and barotropic instability (Hagos and Cook 2007),

and convection over the highland regions (Berry and Thorncroft 2005). Hsieh and Cook (2008) find that convection can strengthen the reversal of the meridional gradient of potential vorticity, causing instabilities that generate easterly waves over West Africa. They suggest that the AEJ plays a role in sustaining the waves even though the instability of the jet may not be their main cause. Berry and Thorncroft (2012) show that organized deep convection embedded within an AEW makes a large contribution to the synoptic-scale mean potential vorticity and therefore to the energetics of the AEW. Their WRF experiment demonstrates that convection is vital for the maintenance of the AEW over West Africa and suggests that AEWs require active convection to persist for an extended length of time.

AEWs regulate the convection initiation and life cycle of ensembles of organized MCSs of long duration throughout the WAM season (Sultan and Janicot 2000). Thus, precipitation triggered and modulated by transient AEWs plays a crucial role in WAM hydrology. Since the seasonal rainfall is so closely tied to AEWs, regional model performance should relate to the representation and simulation of AEWs. Accordingly, modeling the behavior of AEWs is a fruitful application of RCMs, made more meaningful by validation against observational evidence.

In a paper documenting the first-time employment of WRF performance over West Africa for simulating AEWs, Druyan et al. (2009) use National Centers for Environmental Prediction (NCEP) Global Operational Analysis (FNL) forcing for 60 days on a 0.5° grid increment. The authors note both the overestimation of precipitation and the too rapid movement of AEWs during September 2006. Vizy and Cook (2009) downscale European Centre for Medium-Range Weather Forecasts (ECMWF) reanalysis data through WRF, on a 30-km grid increment, to analyze 3–5-day simulations of two tropical storms developing from AEWs during September 2006. Chiao and Jenkins (2010) use WRF as a double-nested (25- to 5-km grid increment) NWP model, driven by NCEP Global Forecast System (GFS) forecasts for 7 days. They analyze 3–5-day simulations of an AEW that developed into Tropical Storm Debbie in August 2006, and find that eliminating the presence of the Guinea Highlands prevents the AEW from developing into a tropical disturbance. Both studies note difficulties with WRF evolving and propagating AEWs for simulations beyond 5 days.

An evaluation of RCM performance must consider alternative model configurations. WRF has become host to many alternative sophisticated parameterizations of physical processes, such as radiation transfer, surface hydrology, boundary layer turbulence, and cumulus

convection. The optimum WRF parameterization combination must be selected for each application and perhaps for each geographic region. The testing and validation of WRF parameterizations is especially important because climate simulations are indeed sensitive to model configuration (Lynn et al. 2009). Flaounas et al. (2011) test six different combinations of two alternative WRF parameterizations for cumulus convection and PBL, in order to optimize the model for simulating the WAM onset during 2006. These authors find a suitable combination that reproduces the general circulation and precipitation regime over West Africa after WAM onset. The current paper takes the optimization step further by analyzing the multiple combinations of five parameterizations, in effect considering 64 different model configurations.

Thus, the objective of this paper is to determine the sensitivity of WRF simulations of weather and climate over West Africa to alternative model configurations. The suggestions of WRF configurations resulting from this evaluation should benefit other investigators planning WRF applications over West Africa. Here, WRF performance is assessed at daily time scales as a first step in evaluating its performance for monthly-to-intraseasonal time scales. The paper focuses on WRF simulation skill with AEW circulations and their associated spatial precipitation patterns when it is driven by reanalysis. This paper reports on circulation simulations while the forthcoming second part of this paper discusses WRF skill in simulating precipitation. The study considers which WRF configurations perform best in simulating the spatiotemporal distribution of AEW vorticity centers. This paper is organized as follows: Section 2 describes sensitivity tests with different WRF physical process parameterizations. The domain and model resolution are given in section 2b. Sections 3a and 3b evaluate simulation results for 64 configurations of WRF parameterization combinations for their relative skill for the 2006 focus period, through a series of common statistic metrics validated against observational evidence from reanalysis and radiosondes. Results are compared with those from an RCM already optimized for West Africa. Section 3c discusses the effect of spinup on model skill and interannual differences in validation scores. Section 4 offers conclusions and some perspectives on this work.

2. Methods and data

a. Simulation period

The current study is based on the simulation of circulation during a 12-day run, from 0000 UTC 2–14 September 2006. Simulations for the parallel period during 10 additional years are analyzed to check the robustness of the results. While testing WRF performance over a 12-day period is not exhaustive, it does provide useful insights. The 12 days represent an observed period during the African Monsoon Multidisciplinary Analyses (AMMA) Special Observing Period 3 (SOP3; Redelsperger et al. 2006) with well-defined AEW troughs with embedded growing and decaying convective activity of various sizes, durations, and intensities (Zipser et al. 2009), including the development of the pre-Helene tropical storm (Franklin and Brown 2008). Simulation results are compared to observations made available for the SOP3 by the National Aeronautics and Space Administration (NASA) field campaign, a recognized subgroup within AMMA, denoted as NAMMA (Zipser et al. 2009). Previous studies have examined this period (Druyan et al. 2009; Vizy and Cook 2009; Chiao and Jenkins 2010; Flaounas et al. 2011), but none examined the sensitivity of WRF simulations to the wide variety of parameterizations available to WRF. The evaluation of a 12-day period allows a rather detailed analysis and description of the daily variability of precipitation and circulation for both simulations and observations.

b. Model configuration

Simulations over West Africa are performed using the Advanced Research core of WRF (WRF-ARW, henceforth WRF), version 3.2.1 (Skamarock et al. 2008), a modeling system designed for both NWP and idealized research simulations. WRF employs the ARW dynamics solver (originally referred to as the Eulerian mass core or solver) developed primarily at NCAR for the fifth-generation Pennsylvania State University–NCAR Mesoscale Model (MM5; Liang et al. 2001). WRF and MM5 differ in their physics schemes, numerical and dynamic options, initialization routines, and the data assimilation package, and there has been no MM5 development since 2005. WRF is a modular, nonhydrostatic, and compressible model that uses the sigma vertical coordinate to better simulate airflow over complex terrain. The configuration used here has 30 terrain-following sigma layers between the earth's surface and the 5-hPa model top. The spatial configuration of the model uses the computational domain of the West African Monsoon Modeling Evaluation (WAMME) initiative (Druyan et al. 2010). Figure 1 shows on a Mercator projection the domain, landmass, and topographic features bounded by 20°S–35°N, 35°W–35°E, and centered at 15°N and 5°W. It spans 394 grid points zonally (in the east-to-west direction) and 312 grid points meridionally (in the south-to-north direction) at a horizontal grid increment of 20 km, covering all of West Africa and part of the North and South Atlantic
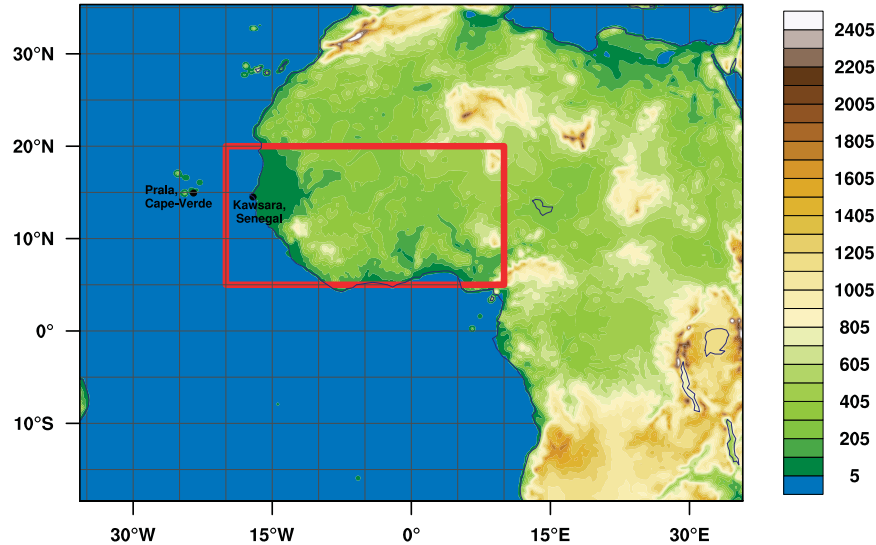
FIG. 1. WRF computational domain with terrain elevation shaded at 100-m intervals. The red box outlines the region validated for vorticity (ζ) variability. The map also shows the two NAMMA radiosonde stations—Praia, Cape Verde and Kawsara, Senegal—used to validate the reanalysis and model 700-hPa meridional wind ($v7$).

Oceans. The red box in Fig. 1 defines a region of AEW activity for which validation statistics are presented in section 3. The most prominent high topography within the box is the Guinea Highlands in the southwest. Figure 1 shows the two NAMMA meteorological radiosonde stations that supply wind data used in the study.

The initial conditions (ICs), lateral boundary conditions (LBCs), and lower boundary conditions, including SST and soil moisture, for all simulations in this study, are specified from the NCEP/Department of Energy Global Reanalysis 2 (hereafter referred to as NCEP2; Kanamitsu et al. 2002). The NCEP2 data are interpolated from pressure levels on a 2.5° Gaussian grid and 6-hourly temporal availability to the WRF grid using the WRF preprocessing system. Reanalysis over data-sparse regions like West Africa provides LBC and validation data that are not always a perfect representation of actual conditions, but the gridded interpolation is nevertheless anchored to and consistent with the observed meteorology. Therefore, driving WRF with NCEP2 ICs and LBCs should represent a high level of potential skill of WRF simulations. No nudging or interactive nesting was used in any of the experiments.

c. Alternative parameterizations

Numerical experiments are designed to the evaluate model performance for different WRF parameterization combinations identified in Table 1. The first column in Table 1 indicates the function of each parameterization,

the second column lists alternative options that are tested in this study, and the third column lists the corresponding acronym for each parameterization option used throughout this text. References for each tested parameterization are given in the fourth column. Multiple alternative WRF parameterizations represent physical processes: CPS, PBL, MPS, LSM, and longwave and shortwave RAD. The WRF development team at NCAR designed the model with modular alternative parameterizations because it is possible that different combinations of parameterizations work better for different applications and regions. Moreover, although convection and microphysics most directly regulate rainfall, convection also affects circulation, so the sensitivity of simulated circulation to CPS is also considered in this study.

This study tests only 64 combinations of WRF parameterizations. Table 2 shows the 64 combinations tested, configured by changing each option one at a time, starting with the first option and its abbreviation listed in Table 1. Configurations are labeled consecutively, 1–64, and are further explained below. Although numerous, the configurations tested here represent a small subset of testable possibilities. In fact, WRF2 (Table 2) is recommended by WRF developers for tropical simulations, (J. Dudhia 2013, personal communication) and is the most commonly used default physics configuration in the WRF literature (see Done et al. 2004; Harrold 2012; Vizy and Cook 2009; Flaounas et al. 2011, 2012). It is very possible that no single WRF configuration is the

TABLE 1. WRF parameterizations considered for all experiments, with abbreviated codes used throughout this study and source citation.

Parameterization	Option	Abbreviation	Citation
Cumulus convection scheme (CPS)	Kain–Fritch scheme	KF	Kain (2004)
	Grell–Devenyi ensemble scheme	GD	Grell (2002)
Planetary boundary layer (PBL)	Yonsei–University scheme	YU	Hong et al. (2006)
	Mellor–Yamada–Janjić scheme	MJ	Janjić (2002)
	Asymmetrical Convective Model, version 2 scheme	A2	Pleim (2007)
	Mellor–Yamada–Nakanishi–Niino scheme	MN	Nakanishi and Niino (2006)
Land surface model (LSM)	Five-layer thermal-diffusion model	5L	Skamarock et al. (2008)
	Unified Noah model	NO	Chen and Dudhia (2001)
	Rapid Update Cycle model	RU	Benjamin et al. (2004)
	Pleim–Xiu model	PX	Pleim and Xiu (2003)
Longwave and shortwave radiation (RAD)	Rapid Radiative Transfer Model for GCMs (RRTMG)	Rt	Iacono et al. (2008)
	Community Atmospheric Model	CM	Collins et al. (2004)
Microphysics scheme (MPS)	WRF single-moment 5-class	W5	Lim and Hong (2005)

best under all circumstances (location, times of day, season, etc.). The reader is referred to Skamarock et al. (2008) for additional details of all parameterizations discussed below.

The CPS represents vertical fluxes from unresolved updrafts and compensating downdrafts outside of clouds and computes the resulting convective precipitation. This study only considers two CPSs. Chiao and Jenkins

TABLE 2. The 64 different WRF combinations of parameterizations included in the sensitivity analysis.

WRF expt	CPS	PBL	LSM	RAD	WRF expt	CPS	PBL	LSM	RAD
1	KF	YU	5L	Rt	33	KF	YU	5L	CM
2	KF	YU	NO	Rt	34	KF	YU	NO	CM
3	KF	YU	RU	Rt	35	KF	YU	RU	CM
4	KF	YU	PX	Rt	36	KF	YU	PX	CM
5	KF	MJ	5L	Rt	37	KF	MJ	5L	CM
6	KF	MJ	NO	Rt	38	KF	MJ	NO	CM
7	KF	MJ	RU	Rt	39	KF	MJ	RU	CM
8	KF	MJ	PX	Rt	40	KF	MJ	PX	CM
9	KF	A2	5L	Rt	41	KF	A2	5L	CM
10	KF	A2	NO	Rt	42	KF	A2	NO	CM
11	KF	A2	RU	Rt	43	KF	A2	RU	CM
12	KF	A2	PX	Rt	44	KF	A2	PX	CM
13	KF	MN	5L	Rt	45	KF	MN	5L	CM
14	KF	MN	NO	Rt	46	KF	MN	NO	CM
15	KF	MN	RU	Rt	47	KF	MN	RU	CM
16	KF	MN	PX	Rt	48	KF	MN	PX	CM
17	GD	YU	5L	Rt	49	GD	YU	5L	CM
18	GD	YU	NO	Rt	50	GD	YU	NO	CM
19	GD	YU	RU	Rt	51	GD	YU	RU	CM
20	GD	YU	PX	Rt	52	GD	YU	PX	CM
21	GD	MJ	5L	Rt	53	GD	MJ	5L	CM
22	GD	MJ	NO	Rt	54	GD	MJ	NO	CM
23	GD	MJ	RU	Rt	55	GD	MJ	RU	CM
24	GD	MJ	PX	Rt	56	GD	MJ	PX	CM
25	GD	A2	5L	Rt	57	GD	A2	5L	CM
26	GD	A2	NO	Rt	58	GD	A2	NO	CM
27	GD	A2	RU	Rt	59	GD	A2	RU	CM
28	GD	A2	PX	Rt	60	GD	A2	PX	CM
29	GD	MN	5L	Rt	61	GD	MN	5L	CM
30	GD	MN	NO	Rt	62	GD	MN	NO	CM
31	GD	MN	RU	Rt	63	GD	MN	RU	CM
32	GD	MN	PX	Rt	64	GD	MN	PX	CM

TABLE 3. Validation data.

Source	Diagnostic	Spatial resolution (°)	Temporal resolution	Period of record	Reference
MERRA	Zonal wind u	1.25	6 h	2–14 Sep 2006	http://gmao.gsfc.nasa.gov/merra
	Meridional wind v	1.25	6 h	2–13 Sep 2006	
	Relative vorticity ($\zeta = \delta v/\delta x$)	1.25	6 h	2–13 Sep 2006	
NCEP2	Zonal wind u	2.5	6 h	2–13 Sep 2006	http://www.esrl.noaa.gov/psd/data/ gridded/data.ncep.reanalysis2.html
	Meridional wind v	2.5	3 h	2–13 Sep 2006	
NAMMA radiosonde at Kawsara, Senegal	Meridional wind v		0–6 × days	2–13 Sep 2006	airbornescience.nsstc.nasa.gov/namma
NAMMA radiosonde at Praia, Cape Verde	Meridional wind v		0–6 × days	2–13 Sep 2006	airbornescience.nsstc.nasa.gov/namma
Regional Model version 3 (RM3)	Zonal wind u	0.5	6 h	2–13 Sep 2006	Druyan et al. (2006)
	Meridional wind v	0.5	6 h	2–13 Sep 2006	
	Relative vorticity ($\zeta = \delta v/\delta x$)	0.5	6 h	2–13 Sep 2006	

(2010) and Lynn et al. (2009) cite GD for short time-scale applications, whereas Patricola and Cook (2010) and Flaounas et al. (2011, 2012) use the KF scheme for longer time-scale applications.

PBL schemes parameterize the unresolved turbulent vertical fluxes of heat, momentum, and constituents such as near-surface moisture flux from the earth surface, wind, ceiling, and visibility within the PBL.

LSMs combine soil-moisture interactions with surface information to calculate the vertical turbulent transport into the PBL. While the Rapid Update Cycle (RUC) LSM scheme prescribes its own distribution of land surface type, vegetation type, and vegetation cover, the other LSM schemes use the WRF default inventories provided by the U.S. Geodetic Survey. Variability in soil moisture feeds back on the atmospheric circulation, strongly affecting the surface-heat budget by partitioning the incoming radiative energy into sensible and latent heat fluxes. LSMs thus supply WRF with energy and water vapor fluxes from the land, and are evaluated here since the previous literature cites that soil-moisture variability occurs during 12–15-day periods (Taylor 2008).

RAD computes atmospheric heating from the radiative flux divergence. This paper tests two RAD schemes intended for climate simulations. The first RAD is the Rapid Radiative Transfer Model for GCMs (RRTMG or Rt), adapted from the MM5, and includes the Monte Carlo independent-column approximation with random cloud overlap for representing subgrid-scale cloud variability (Iacono et al. 2008). Flaounas et al. (2011, 2012) uses the Rt for intraseasonal simulations of the WAM onset. The second RAD is derived from the Community Atmosphere Model (CM), the atmospheric component of NCAR Community Earth System model. WRF configurations 1–32 in Table 2 (left-hand side) each use the Rt, and configurations 33–64 (right-hand side) use the CM.

MPS explicitly resolves water vapor, cloud, and precipitation processes. Pohl et al. (2011) and Crétat et al. (2012) find that MPSs exert a minor influence on rainfall characteristics (location, intensity, and number of rainy events) over eastern and southern Africa. Among the MPS options in WRF are a series of WRF single-moment schemes: the 3-class, 5-class (WSM5), and 6-class (WSM6) versions are widely used (Hong et al. 2004). Both WSM5 and WSM6 are suitable for domain resolutions less than 25 km (Hong et al. 2006). This study adapts the computationally less expensive choice: WSM5 (W5). Table 2 does not show MPS since the WSM5 is used in all WRF configurations.

d. Validation datasets

Table 3 describes the validation datasets used to assess the skill of the simulations. Model results are compared to two different reanalysis datasets. Reanalysis data are anchored to the observed meteorology, but in data-sparse regions like West Africa, much weight is given to the analysis model simulation. WRF-modeled zonal and meridional wind is compared to the NASA Modern-Era Retrospective Analysis for Research and Applications (MERRA; Rienecker et al. 2011). It has global coverage with a horizontal grid increment of 1.25° × 1.25°. MERRA assimilates observational datasets, including those from space-based platforms, and offers more diagnostic parameters than any other reanalysis to date. WRF results are also compared to the reanalysis dataset used as ICs and LBSs, the NCEP2 (Kanamitsu et al. 2002).
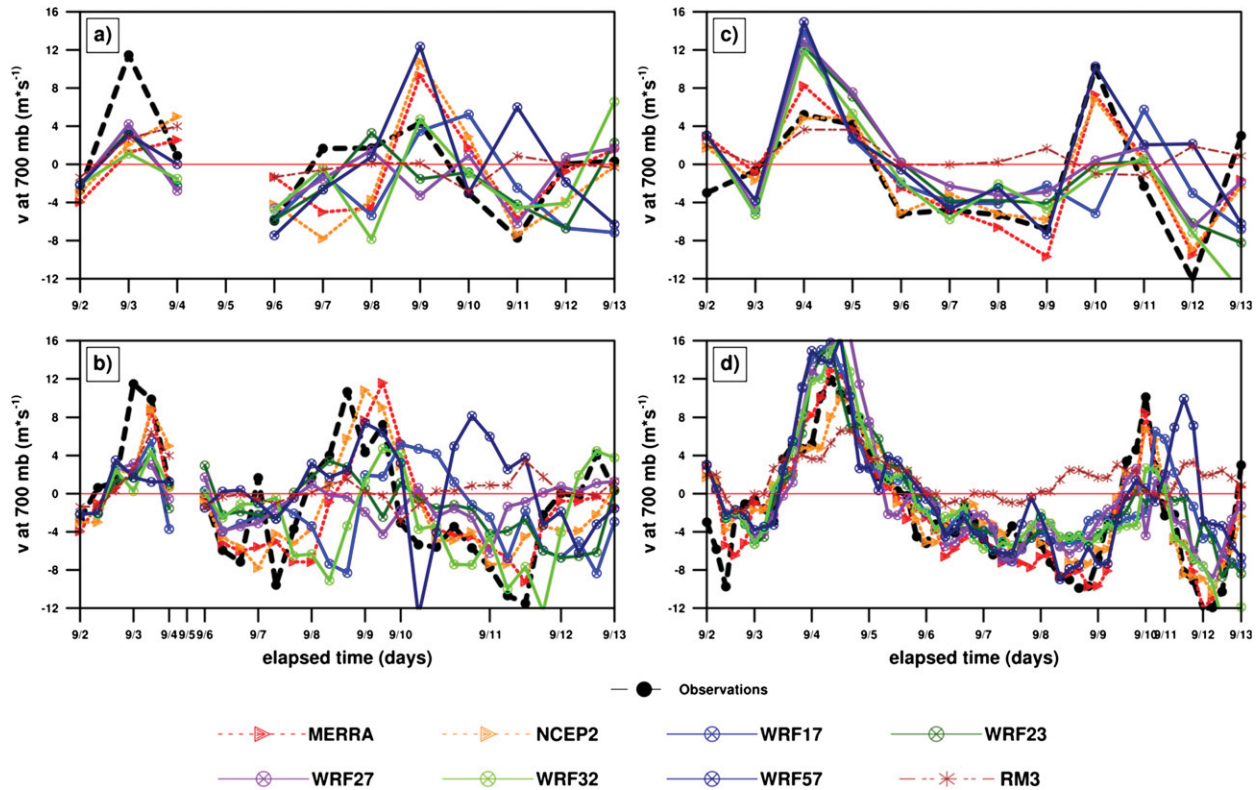
FIG. 2. Time series of NAMMA radiosonde observations of 700-hPa meridional wind ($v7$) collected from (a),(b) Kawsara, Senegal, and (c),(d) Praia, Cape Verde, for the WRF configurations from Table 4, RM3, MERRA, and the NCEP2 reanalysis at (top) 0000 UTC and (bottom) all-time (see text).

WRF circulation data are additionally compared to NAMMA radiosonde observations over Kawsara, Senegal, and Praia, Cape Verde. Kawsara radiosondes were released specifically for storm events, resulting in 72 radiosondes released 0–6-times per day from 15 August to 16 September 2006 (Delonge 2013). Praia radiosondes were released 4-hourly from 18 August to 9 September, and then 6-hourly on 10–14 September 2006 (Schmidlin 2013).

AEWs propagate zonally, creating strong time variations in the meridional component v of the lower and midtropospheric wind (Reed et al. 1988). We check how well MERRA and NCEP2 represent the circulation by comparing 700-hPa v ($v7$) in each dataset to two sets of NAMMA radiosonde observations. Figure 2a shows the time series of $v7$ over Kawsara, (black-dashed line), from radiosondes released between 0000 and 0600 UTC, comparing them to 0000 UTC $v7$ from MERRA (red line with triangles), NCEP2 (orange line with triangles), WRF17, WRF23, WRF27, WRF32, WRF53, and RM3 (see below). WRF configurations are selected from the analysis in section 3. Figure 2b shows observations at "all-time" compared to reanalysis and modeled $v7$. Correlations between the time series in Fig. 2b, labeled

all-time in Table 4, are computed by pairing each reanalysis or model $v7$ with the radiosonde observation that is closest in time (but never more than 3 h earlier or later). Kawsara observations are missing for 5 September. Figures 2c and 2d show similar comparisons over Praia.

Figure 2a shows that MERRA and NCEP2 capture $v7$ variability associated with two AEWs, but delay the $v7$ shift to southerlies by 48 h on 6–8 September. It shows some WRF configurations and RM3 outperforming MERRA and NCEP2 for 6 days, then diverging from the 8 September observations, then recovering the observed $v7$ shifts as an AEW approaches Kawsara on 9–11 September. Table 4 shows similar correlation scores for both the Kawsara 0000 UTC and the all-time analysis, except that the latter improves the correlations for the reanalyses. WRF27 outperforms all the models in both Kawsara comparisons ($r = 0.69$ and 0.60, respectively), whereas RM3 performs third best in the 0000 UTC analyses, but shows no correlation with observations over Kawsara in the all-time analysis.

Figures 2c and 2d and Table 4 show that both reanalyses and the models simulate the observed $v7$ variability over Praia quite well. Results imply that either

TABLE 4. Correlations between the time series in Fig. 2b: comparisons of AMMA radiosonde observations of $v7$ collected at 0000 UTC and all-time against collocated modeled $v7$ from WRF configurations from Table 2, RM3, MERRA, and NCEP2 reanalysis. Correlations between the time series labeled all-time are computed by pairing each reanalysis or model $v7$ with the radiosonde observation that is closest in time (but never more than 3 h earlier or later).

Kawsara, Senegal			
Model	r (0000 UTC)	Model	r (all-time)
WRF27	0.69	MERRA	0.71
WRF23	0.62	NCEP2	0.71
RM3	0.49	WRF27	0.47
NCEP2	0.47	WRF32	0.45
MERRA	0.43	WRF23	0.44
WRF32	0.43	RM3	0.30
WRF17	0.38	WRF57	0.12
WRF57	0.33	WRF17	0.04
Praia, Cape Verde			
Model	r (0000 UTC)	Model	r (all-time)
NCEP2	0.90	MERRA	0.91
MERRA	0.87	NCEP2	0.91
WRF27	0.60	WRF27	0.79
WRF57	0.54	WRF32	0.78
WRF23	0.48	WRF23	0.74
WRF32	0.38	WRF17	0.72
WRF17	0.22	WRF57	0.64
RM3	0.05	RM3	0.47

reanalysis is representative of the observed wind variability and is therefore appropriate for validating model performance. Table 4 also shows that WRF27 and WRF32 outperform the other models. The higher WRF scores over the ocean could suggest that AEWs are simulated more accurately over prescribed SSTs, remote from imperfectly modeled land–atmosphere interactions. Figures 2c and 2d show the very low $v7$ variability of the RM3 during the last 6 days and, as a result, Table 4 shows it underperforming all of the models over Praia.

To better appreciate WRF's potential for evolving West African weather patterns, results from another model are presented as a benchmark. The 12-day 2006 simulation over the same domain and forced by the same lateral boundary conditions is repeated using the NASA Goddard Institute for Space Studies and Center for Climate Systems Research Regional Model version 3 (NASA GISS/CCSR RM3; hereafter RM3) on a 0.5° grid. The RM3 has previously been used to study AEWs (Druyan et al. 2006, 2009) and longer-term climate simulations in the WAMME initiative (Druyan et al. 2010), another recognized subgroup within AMMA. Druyan et al. (2010) summarize WAMME results from five RCMs simulating the WAM with both reanalysis and GCM forcing, where the RM3, Met Office Hadley Centre

RCM (HadRM3P), MM5, and the Regional Climate Model (RegCM3) show a range of skill in simulating seasonal mean zonal wind and meridional moisture advection. MM5 and HadRM3P are shown to overestimate moisture convergence over West Africa. The study does not include WRF.

3. Results

a. Simulation of AEWs

Reed et al. (1988) introduced the method of using 700-hPa relative vorticity fields to identify AEW tracks in ECMWF reanalysis data. Here, we consider the zonal gradient of v ($\zeta = \delta v/\delta x$), a modified configuration of the relative vorticity tracking method introduced by Hodges (1995) and Thorncroft and Hodges (2001) that neglects the background contribution of $\delta u/\delta y$.

Figure 3 depicts a series of wave troughs and ridges, represented by 700-hPa ζ ($\zeta7$) maxima and minima, on three consecutive days. Figure 3 compares MERRA (top three panels) and WRF27 (bottom three panels) 700-hPa total wind (V7) vectors superimposed over horizontal distributions of $\zeta7$ at 0000 UTC 10–12 September 2006, during which three of the four AEWs, designated as AEW2, AEW3, and AEW4 in subsequent figures, traversed the region. AEW1 is not shown. The $\zeta7$ maxima indicate the positions of inverted troughs, and thus the axis of each AEW, while the V7 vectors outline the shape of each 700-hPa trough. WRF27 is shown here because it achieves relatively high validation scores for vorticity (see below) and precipitation (not shown). Figure 3a identifies the MERRA AEW2 $\zeta7$ maximum and its V7-vector trough axis at 25°W, and a corresponding WRF27 shallower trough is shown in Fig. 3b. The MERRA AEW3 propagates westward from 7°N, 7°W (Fig. 3c) to 10°N, 20°W (Fig. 3e), and the corresponding WRF27 AEW3 shows a similar track in Figs. 3d–f except for a slight northward displacement. A noticeable difference between WRF and MERRA is that the intensity of the AEW3 trough decreases with time in the simulation, while it increases in MERRA. AEW4 is near 18°E on 10 September, eventually reaching 5°E by 12 September, while the WRF27 AEW4 lags by several degrees to the northeast. In this example, WRF27 generates the major MERRA $\zeta7$ centers and corresponding westward tracks, but several position displacements and time lags are evident.

In Fig. 4, $\zeta7$ centers with closed contours of at least $+0.5 \times 10^{-5}\,s^{-1}$ locate $\zeta7$ maxima in order to trace AEW tracks during the 12-day period. Tracks based on MERRA (black lines), NCEP2 (red lines), and WRF27 (blue lines) show the paths of AEW1, AEW2, AEW3, and AEW4 (Figs. 4a–d, respectively). Differences between the
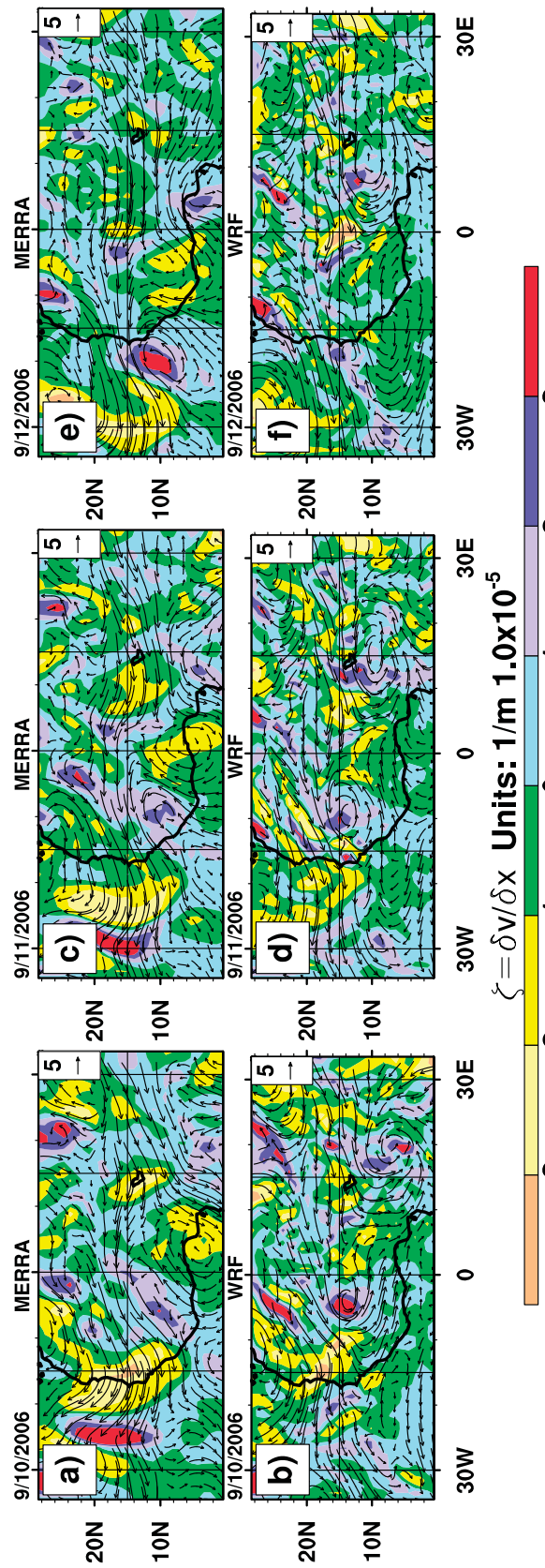
FIG. 3. The 700-hPa vorticity ($\zeta 7$) overlaid with 700-hPa wind (V7) vectors (m s^{-1}): a comparison between (a),(c),(e) MERRA and (b),(d),(f) WRF27 at 0000 UTC on (left to right) each day 10–12 Sep 2006. The $\zeta 7$ maxima (blue–red areas) represent AEW trough centers.
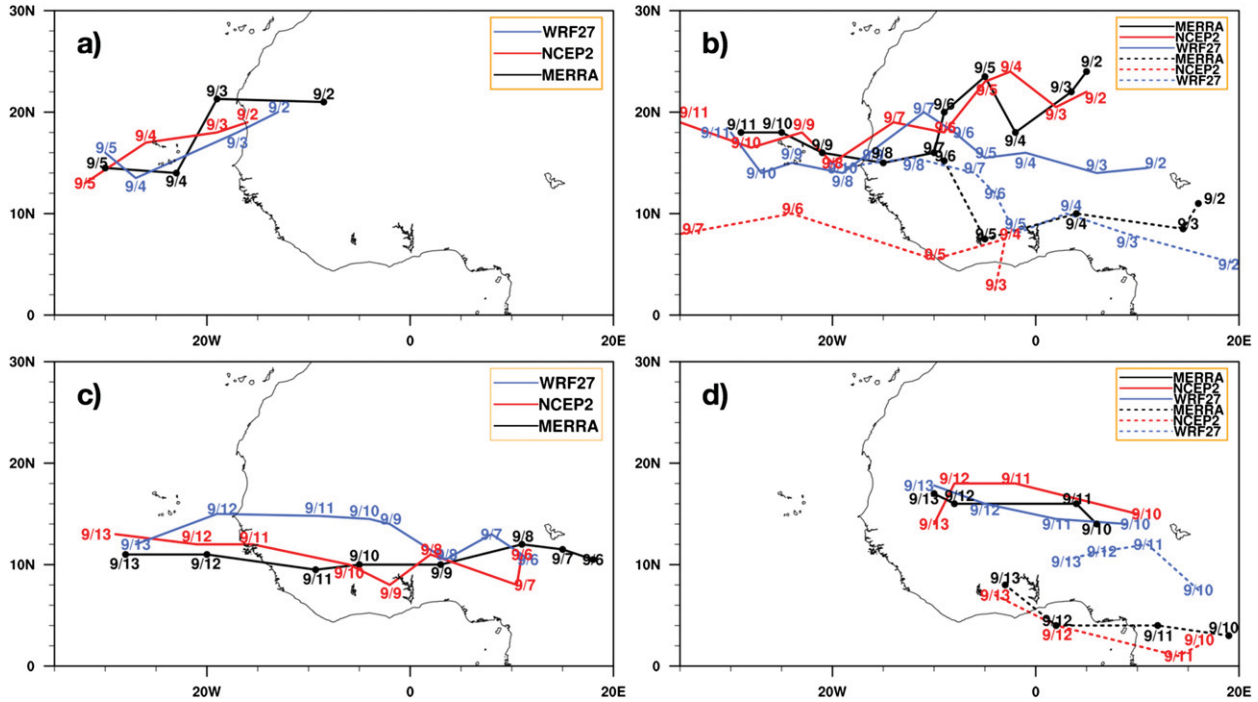
FIG. 4. AEW tracks at 700 hPa plotted using ζ7-maxima centers at 0000 UTC on each day for WRF27 (solid and dashed blue lines), MERRA (solid and dashed black lines), and NCEP2 (solid and dashed red lines): (a) AEW1, (b) AEW2, (c) AEW3, and (d) AEW4. Solid lines are only in (a),(c).

MERRA and NCEP2 tracks testify to their uncertainty and perhaps to the effect of resolution. Figure 4b shows that, by all accounts, AEW2 appears as two waves that eventually merge on 8 September, a typical AEW characteristic (see Reed et al. 1988). NCEP2 does not merge the two waves at all. Analysis of the tracks in Fig. 4c shows that all three datasets detect AEW3 on 6 September and move it to the Atlantic by the end of the period. The WRF AEW3 track is displaced to the north of the reanalyses tracks during 9–12 September. Figure 4d shows the paths of two AEWs that merge into AEW4 on 14 September 2006 (not shown). The northern track simulated by WRF27 is similar to both reanalyses, but the modeled southern track strongly differs from the reanalysis. The simulated southern wave is located too far north (especially during 11–12 September), and it propagates westward too slowly. Moreover, WRF27 maintains the separation of the two waves, whereas both reanalyses begin merging the waves together into AEW4 on 14 September (not shown). Based on all four AEW tracks, the area from 5° to 20°N and from 10°E to 20°W is selected for further investigation of the ζ7 diagnostic, using Hovmöller diagrams discussed in the remainder of this section.

An alternative method for examining the progression of AEWs through the Sahel region involves the use of

the Hovmöller diagram, which allows for an evaluation of spatiotemporal variability on the same chart (see Hovmöller 1949; Martius et al. 2006), but also incorporates some spatial averaging. In this study, the diagnostic is used to compare the zonal movement, or swaths, of v7 and ζ7 from the WRF configurations, to reanalysis.

Figure 5 shows three time–longitude Hovmöller diagrams of v7 on the left-hand side and three ζ7 on the right-hand side for each day, 2–13 September 2006, at 0000 UTC. The data represent averages over 5°–20°N. The x axis indicates longitude, and the y axis indicates elapsed time. Figures 5a and 5b show data fields for MERRA, Figs. 6c,d for WRF27, and Figs. 6e,f for RM3. Figures 5a, 5c, and 5e show that v7 modulates from northerlies (blue contours) to southerlies (yellow-orange contours) with the progression of time and longitude across the region. The darkened zero-line contours, with northerlies to the left and southerlies to the right, indicate the position of the v7 troughs. While the v7 wind reversals provide a clear indication of AEW movement, swaths of ζ7 maxima in Figs. 5b, 5d, and 5f more objectively define daily positions of AEW. Note that the v7 troughs on the left-hand side are collocated with the position of the AEW axis of positive ζ7 on the right-hand side. Figure 5a shows three MERRA v7 troughs propagating westward
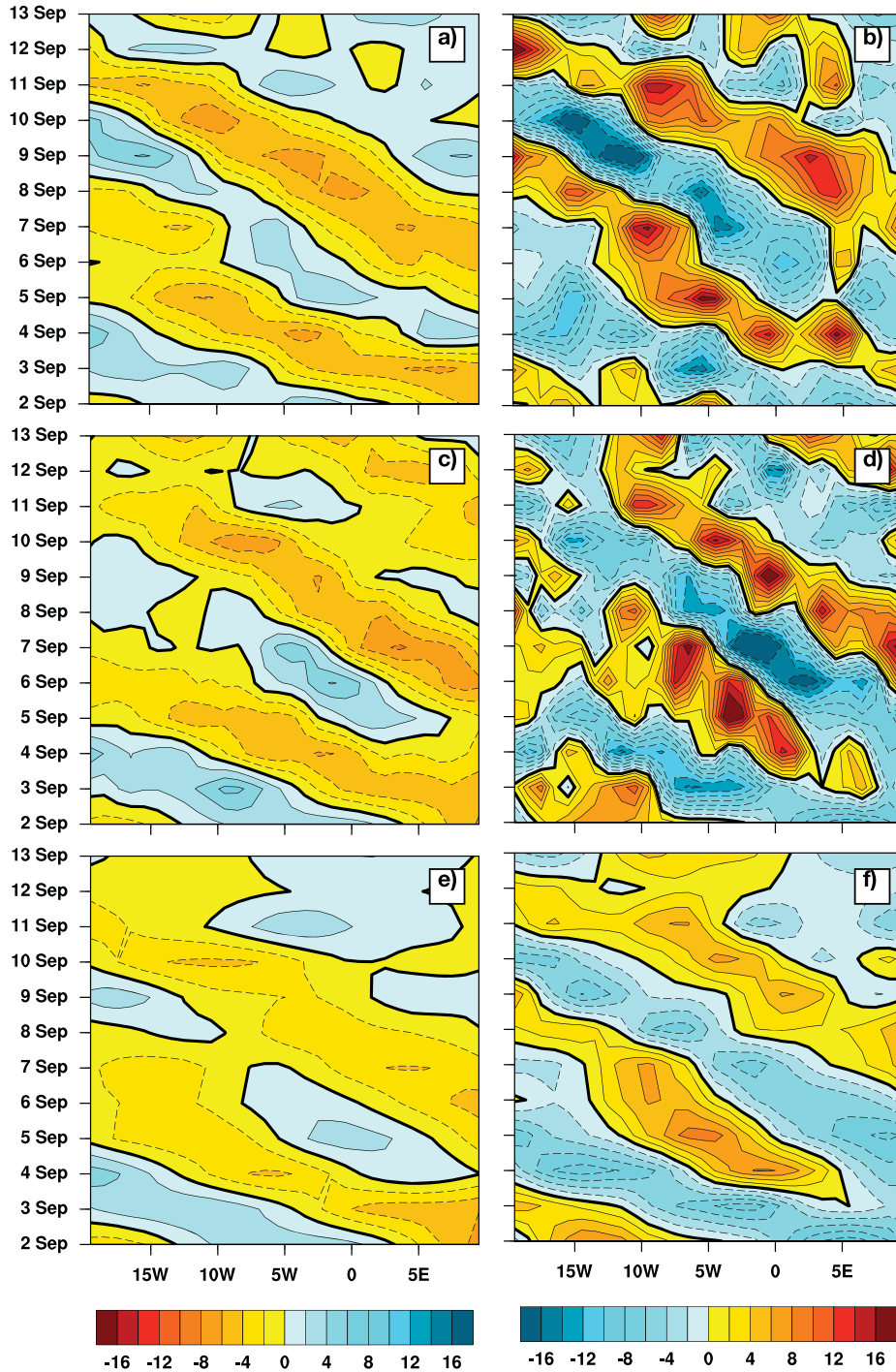
FIG. 5. (left) Time–longitude Hovmöller distributions of $v7$ (m s^{-1}). The zero-line contours, with northerlies to the left and southerlies to the right, indicate the position of the $v7$ troughs. (right) Hovmöller distributions of $\zeta 7$ (s^{-1}). Both diagnostics are plotted at 0000 UTC on the designated days (y axis), 2–13 Sep, and averaged over 5°–20°N for (a),(b) MERRA, (c),(d) WRF27, and (e),(f) RM3.

across all longitudes and a less well-defined fourth $v7$ trough from 10 September through 13 September, whereas Fig. 5b clearly shows all four AEWs. MERRA's AEW2 swath, in Fig. 5b, propagates from outside 10°E on 3 September and shows evidence of two maxima (as discussed for Fig. 4), between 5°E and 1°W, propagating to 20°W on 9 September and implying a wave speed of approximately 5 m s^{-1}. MERRA's AEW3 swath
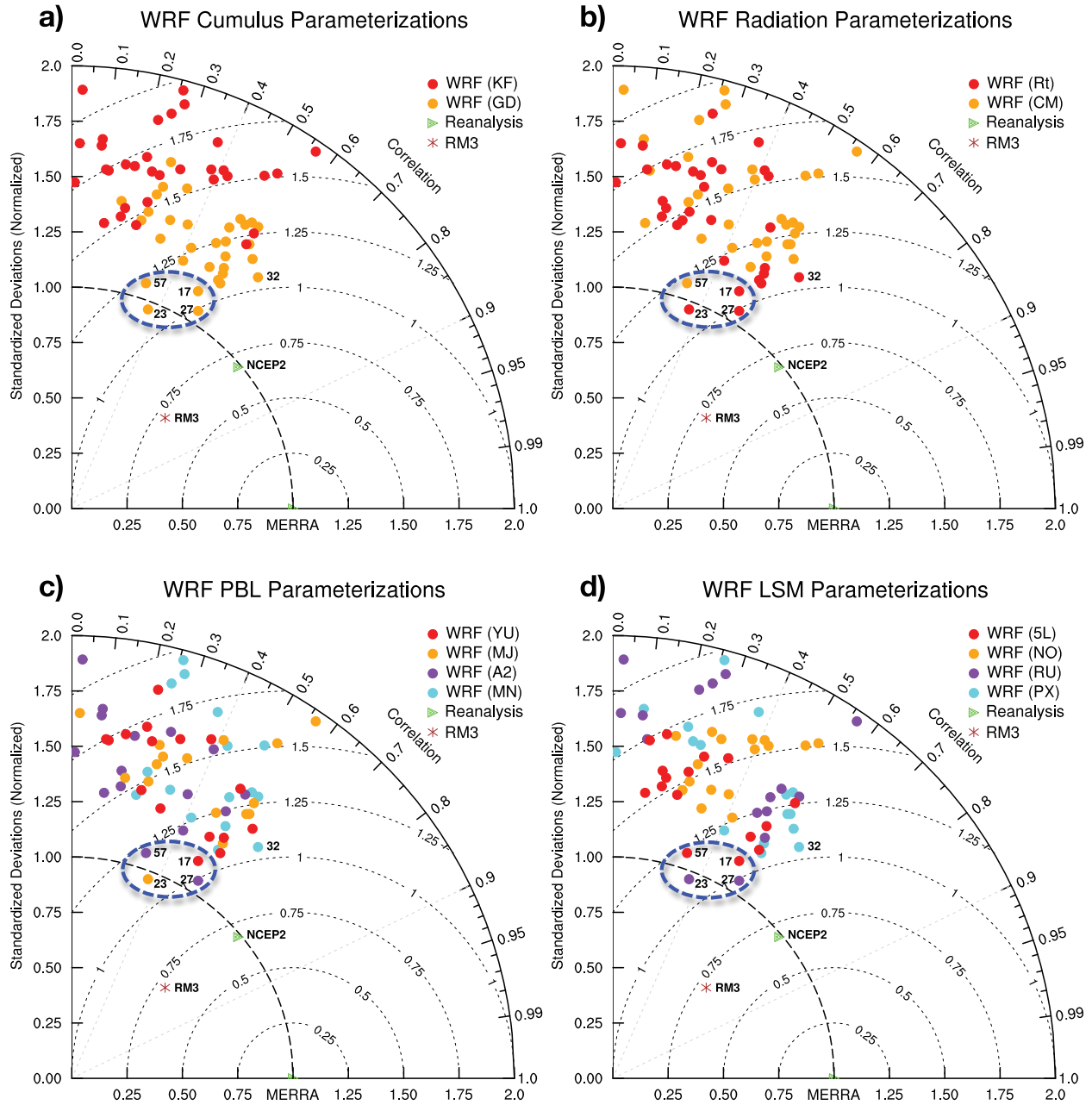
FIG. 6. Validation scores for the time–longitude Hovmöller distributions of $\zeta 7$ (as in Fig. 6, right), for each of 64 WRF experiments compared to MERRA. In these Taylor diagrams, values along radial spokes indicate the correlation r and values of concentric arcs indicate σ normalized by MERRA standard deviations σ_n. The dashed semicircles measure the normalized RMSE centered differences between each point and MERRA. Colors (see legends) differentiate between major WRF parameterizations used in each experiment (see Table 2): (a) CPS, (b) RAD, (c) PBL, and (d) LSM. The best WRF scores are highlighted by the dashed blue oval.

propagates from outside 10°E on 7 September to 20°W on 12 September, implying a wave speed of approximately of $7.5 \, \mathrm{m \, s^{-1}}$. Corresponding WRF27 swaths are evident in Fig. 5d, but there are disagreements in their path and timing. Figures 5e and 5f show that RM3 swaths have weaker $v7$ and $\zeta 7$ extremes than either WRF27 or

MERRA. However, RM3 $\zeta 7$ maxima and corresponding $v7$ extremes associated with the AEW1, AEW2, and AEW3 tracks are closely aligned with those of MERRA. The circulation associated with AEW4, on the other hand, is more poorly reproduced by RM3. Performance scores are quantified in the following discussion.

Time–longitude Hovmöller distributions of $\zeta 7$ are constructed for each of the 64 WRF experiments in Table 2 and then compared to the corresponding MERRA Hovmöller distribution. The validation of the Hovmöller time–longitude distributions of simulated versus observed $\zeta 7$ provides statistics that evaluate temporal and longitudinal variability. Each WRF simulation is compared to the reanalysis using statistical skill scores of cross correlation r, RMSE, and standard deviation σ. All WRF and observed circulation results are compared on a $1° \times 1°$ grid using the first-order conservative-remapping method.

A Taylor diagram provides a visual framework for a statistical summary of how well patterns match each other in terms of their RMSE, r, and the ratio of their σ, concurrently, in one plot (Taylor 2001). Figure 6 graphically summarizes the skill scores between the modeled and MERRA $\zeta 7$ Hovmöller distributions. In Fig. 6, the radial distance from the origin measures the magnitude of each σ_n, normalized by dividing by the corresponding MERRA σ value. The normalized RMSE-centered difference between each point and MERRA is measured by the values of the dashed semicircles. The spatial r, WRF versus MERRA, is given by the azimuthal position of each point, labeled along the outer arc. Figures 6a–d not only allow us to evaluate model data performance by characterizing the statistical relationship between modeled and observed $\zeta 7$, but they also help us investigate the modeled $\zeta 7$ sensitivity to alternative components. The Taylor distribution of statistics is shown four times: in each panel a different WRF parameterization from Tables 1 and 2 is highlighted to examine its influence on the scores. Figure 6a does this for CPS, Fig. 6b does this for RAD, Fig. 6c does this for PBL, and Fig. 6d does this for LSM.

NCEP2 scores the best σ_n (0.99) and r (0.77), which means that comparisons between the WRF experiments versus MERRA should be analogous to comparisons with NCEP2. The Taylor diagram shows that the RM3 scores a similar r to NCEP2 (0.73), which is the highest r among all the regional models. However, its rather low σ_n (0.59) indicates that it underestimates the spatiotemporal variability of $\zeta 7$ compared to MERRA. The WRF experiments validate with a range of scores, where several experiments achieve statistically significant r between 0.40 and 0.63 and a σ_n close to unity. The majority of the WRF simulations score a $\sigma_n > 1.10$, meaning that WRF produces somewhat more $\zeta 7$ variability than MERRA. The four WRF configurations that score both the best σ_n and high r values are enclosed within the blue circle (WRF17, WRF23, WRF27, and WRF 53). WRF32 is noted because it scores the highest r among the WRF simulations. Changing the CPS parameterization from

KF to GD (Fig. 6a) produces an unambiguous improvement in the scores of many WRF configurations, achieving most of the highest r and best σ_n values. In addition, three out of the four best scorers use the RT RAD rather than the CM (Fig. 6b). Otherwise, some high-scoring configurations incorporate alternative parameterizations of PBL and LSM, implying that their influence is ambiguous. However, no configuration with MN PBL (Fig. 6c) or A2 LSM (Fig. 6d) is found in the circle of the best four, and all of the configurations with the NO LSM performed poorly.

The aforementioned r scores validate performance over all 12 days. However, simulations with lower r scores often reflect larger $\zeta 7$ track displacements from MERRA positions on individual days (not shown). For example, the WRF32 (12-day $r = 0.67$) simulated AEW3 $\zeta 7$ maximum was 1.9° closer to the MERRA position than the WRF2 (12-day $r = 0.35$) simulation on 9 September, 2.2° closer on 10 September, and 5.7° closer on 11 September 2006 (0000 UTC). Figure 7 shows another aspect of WRF performance for individual days.

Figure 7 examines the daily changes in validation scores of five WRF configurations selected as promising from Fig. 6 and the RM3. It shows daily cumulative r, validating Hovmöller $\zeta 7$ distributions up to and including the day indicated, between modeled $\zeta 7$ for WRF17, WRF23, WRF27, WRF32, WRF53, and RM3 versus MERRA (blue line) and NCEP2 (solid green line). Figure 7 also shows daily r values, validating results specific to each day, between the same WRF configurations versus MERRA (red line) and NCEP2 (orange line). The daily r value specific to each day shows whether the simulation for an individual day was skillful or not, which cannot be deduced from the cumulative r values. WRF configurations score statistically significant cumulative r values throughout the 12 days. (Note that the cumulative r against MERRA at 0000 UTC 13 September is the r score given in Fig. 6.) Furthermore, the WRF versus MERRA and WRF versus NCEP2 cumulative-r trends are identical. Figure 7f shows that the RM3 versus NCEP2 cumulative r is higher than for any of the WRF configurations, and higher than r against MERRA, in contrast to the WRF configurations validating similarly against both reanalyses. The daily r values between the WRF configurations and reanalysis start and remain significantly high out to 9 days, but fall steeply by the 10th day, followed by a relatively low score on the 11th day, when the models retard the propagation of AEW3 and AEW4 compared to the reanalysis, as seen in Figs. 3–5. The peaks and the minimums for each WRF configuration often occur on the same day, indicating that the configurations have similar performance
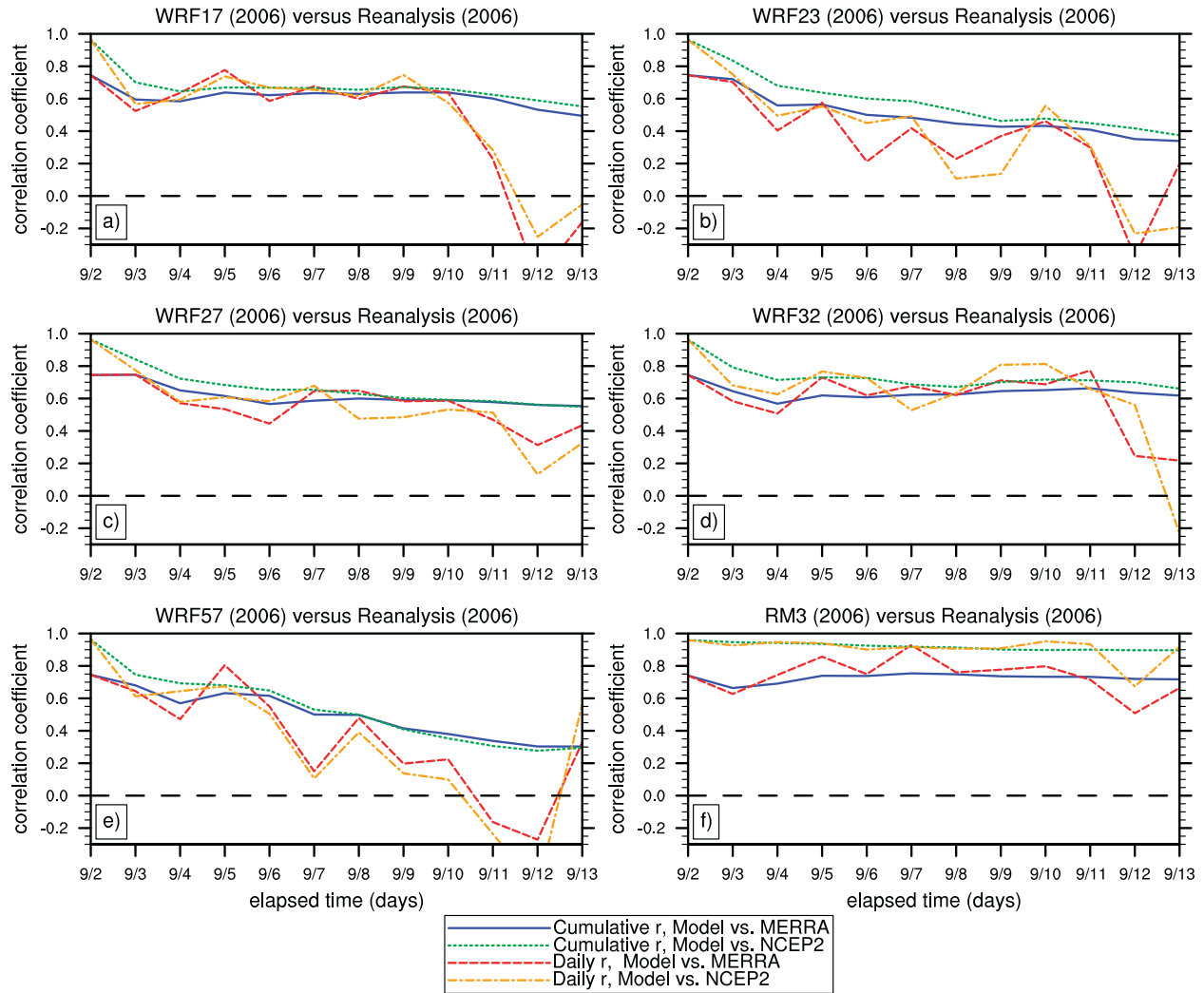
FIG. 7. Time series showing two aspects of correlation r of the WRF modeled $\zeta7$ from the five WRF configurations selected as promising from Fig. 6, against the MERRA and NCEP2 reanalysis $\zeta7$, valid at 0000 UTC for each day. The cumulative r values between the models and MERRA (solid blue line) and NCEP2 (dotted green line) validate results up to and including the day indicated. The daily r value between the models and MERRA (dashed red line) and NCEP2 (dashed orange line) validates results specific to that day for (a) WRF17, (b) WRF23, (c) WRF27, (d) WRF32, (e) WRF53, and (f) RM3.

characteristics. This implies that WRF uses information from the LBC to simulate AEWs with similar timing and tracks as in the reanalysis for about 10 days. However, the performance of WRF may be sensitive to the synoptic-scale configuration of a particular day and its representation by the forcing data, in addition to model physics.

b. Simulation of mean zonal winds

Insight into model performance can be gained by examining zonal wind structure. The simulation of the AEJ is of interest because AEWs derive energy from the jet (Hsieh and Cook 2008) and AEJ core speeds propel AEWs westward. Strong meridional soil-moisture

gradients lead to strong positive meridional-temperature gradients at the surface and in the lower troposphere (Cook 1999). Thus, surface heating over the Sahara Desert sets up a positive meridional-temperature gradient between the equator and 25°N. The positive meridional-temperature gradient at the surface causes vertical wind shear, which induces easterly flow at midlevels overlying the surface monsoon WA westerly jet (Cook 1999). Figure 8 shows the 0000 UTC 12-day mean of the zonal winds u along the north–south 0° transect, plotted with the corresponding cross section of potential temperature θ. Figure 8a shows MERRA, Fig. 8b shows NCEP2, and Fig. 8c shows the WRF2. Figures 8e and 8f show WRF17, WRF27, and WRF32, respectively, which
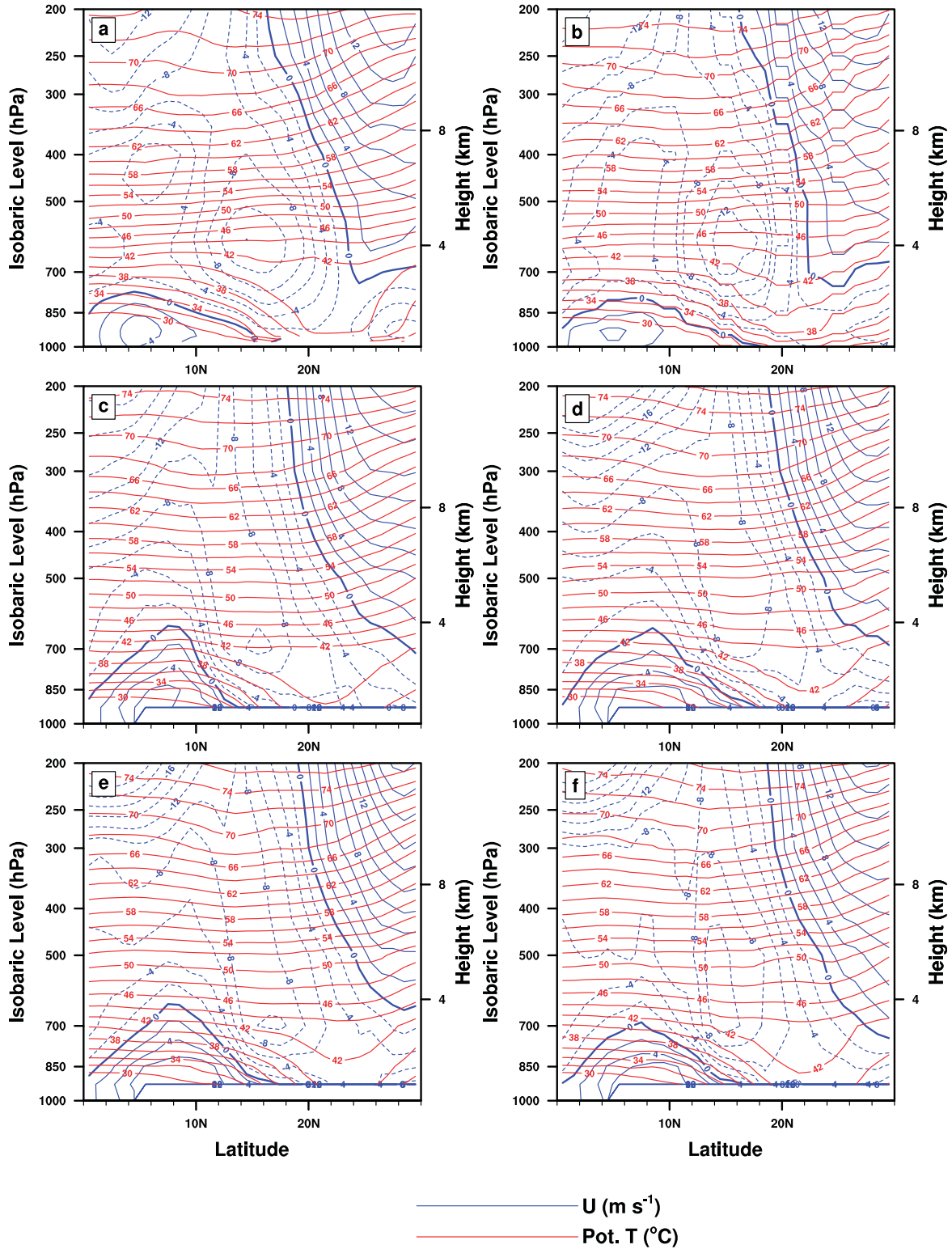
FIG. 8. The 12-day means of the 0000 UTC zonal winds (u, blue) along a north–south transect at 0° plotted with the corresponding cross section of potential temperature (θ, red) for (a) MERRA, (b) NCEP2, (c) WRF2, and the WRF default configuration; and three WRF configurations selected as promising from the analysis in Figs. 6: (d) WRF17, (e) WRF27, and (f) WRF32.

are three configurations that validate best against 2006 reanalysis data for 700-mb meridional wind and relative vortices.

Examination of MERRA and NCEP2 u (Figs. 8a,b) shows that the vertical wind shear of the zonal circulation creates a core of strong midtropospheric easterlies featuring an AEJ peak at 600 hPa over 15°N with a core speed of $12 \, \mathrm{m \, s^{-1}}$. Of the two, the NCEP2 core speed is slightly higher. Also evident in the cross section is the reanalysis WA westerly jet in the lowest layers, which gets weaker with altitude and reverses sign near 850 hPa. AEWs that zonally traverse WA largely occur in this zone of vertical shear between the WA westerly jet and the AEJ, and derive energy from the AEJ. The θ contours show a positive northward θ gradient below the AEJ that is consistent with the implied east-to-west shear below the AEJ altitude. MERRA features a prominent, deep, well-mixed PBL between 20° and 24°N, represented by a near-zero vertical lapse up to 700 hPa, the height that coincides with the height of the AEJ. The θ contours also show a weak sign reversal in the meridional θ gradient above the AEJ, which causes a reversal of the thermal wind direction.

The WRF cross sections in Figs. 8c–f differ from the reanalysis by featuring unrealistically strong southern-monsoon westerlies (SMW) within a monsoon layer that is too deep, stretching up to 650–700 hPa. Additionally, the strongest easterlies representing the AEJ core are displaced from 600 to 700 hPa in WRF2 and WRF27, creating an unrealistic horizontal wind shear zone between the deep monsoon layer and the AEJ. This exaggerates the background vorticity at 700 hPa, where AEWs are active. The WRF AEJ core speeds are $2 \, \mathrm{m \, s^{-1}}$ weaker than observed. The WRF simulations show weak vertical shear above the core of the AEJ, unrealistically stretching the AEJ core. The WRF θ contours are similar to MERRA; they show strong positive northward temperature gradients at the surface and in the lower troposphere and a deep and well-mixed boundary layer at 20°–24°N. Major zonal wind features of many other WRF experiments (not shown) are similar to those in Figs. 8c–f.

c. Spinup and multiyear validation

Druyan et al. (2006) report that RM3 precipitation simulations undergo an initial 5-day adjustment period before results compare well with Tropical Rainfall Measuring Mission (TRMM)-observed precipitation variability. Due diligence suggests that any potential benefit of a similar spinup on WRF performance should be tested. Validation statistics of the Hovmöller $\zeta 7$ distributions for the 6 days (7–13 September 2006) are in fact less favorable than for the first 6 days (not shown; 2–7 September 2006), suggesting that elapsed time degrades simulation performance. The

low scores for 12 September, discussed above (Fig. 7), likely affect these results. We also compare the scores for the WRF configurations in Table 4 with scores for simulations initialized on 27 August, but validated for the same 12-day study period. Results (not shown) also indicate that a 6-day spinup does not improve the performance, even over the entire period of the control run.

The WRF17, WRF23, WRF27, WRF32, and WRF53 simulations are repeated with NCEP2 boundary conditions for the remaining years, 2000–10. Figure 9 shows cumulative r values versus elapsed time for the Hovmöller $\zeta 7$ distributions for simulations of all 11 yr. Comparison of NCEP2 to MERRA (Fig. 9a) shows that the validation between the two reanalyses is practically identical and consistently high for each year (with a range in r of 0.5–0.8). Note that there is a large range of scores for the 11 yr in Figs. 9b–f. Correlations remain useful until the end of the period during just 2006, implying that only in that case does information from the LBC create AEWs with similar timing and tracks as MERRA. However, simulations with data from most years rapidly lose correlation after the first day. The highest r for other years is 0.80 for 2005, but registered only during the first 72 h.

Figure 10 is similar to Fig. 9, except that it shows the 2005 and 2010 r scores for the five selected WRF configurations from Fig. 6. The WRF configurations achieve scores of 0.80 during the first 72 h in 2005, in contrast to rapidly declining r after the first day in 2010. This performance is considerably inferior to that discussed above for the 2006 simulations.

Reasons for the superior 2006 performance compared to that of other years are not obvious. The quality of the simulations may be somewhat dependent upon the particular synoptics of a given year, just as WRF performance was shown to suffer for 12 September 2006 (see above). We also note that the AMMA-SOP3 field campaign occurred during August–October 2006. Perhaps the enhancement of field observations enriched the database in the region for the NCEP and MERRA reanalyses used here, respectively, for boundary conditions and for validation. AMMA radiosonde data were made available to weather centers during AMMA. AMMA-SOP3 field data were apparently assimilated into NCEP2, although their impact was not assessed (W. Thiaw 2013, personal communication).

4. Discussion and conclusions

The performance of WRF as a regional atmospheric model run on a 20-km grid over West Africa is evaluated from more than a hundred 12-day simulations in September during 11 consecutive years. The study focuses on the simulation of the mean wind structure and
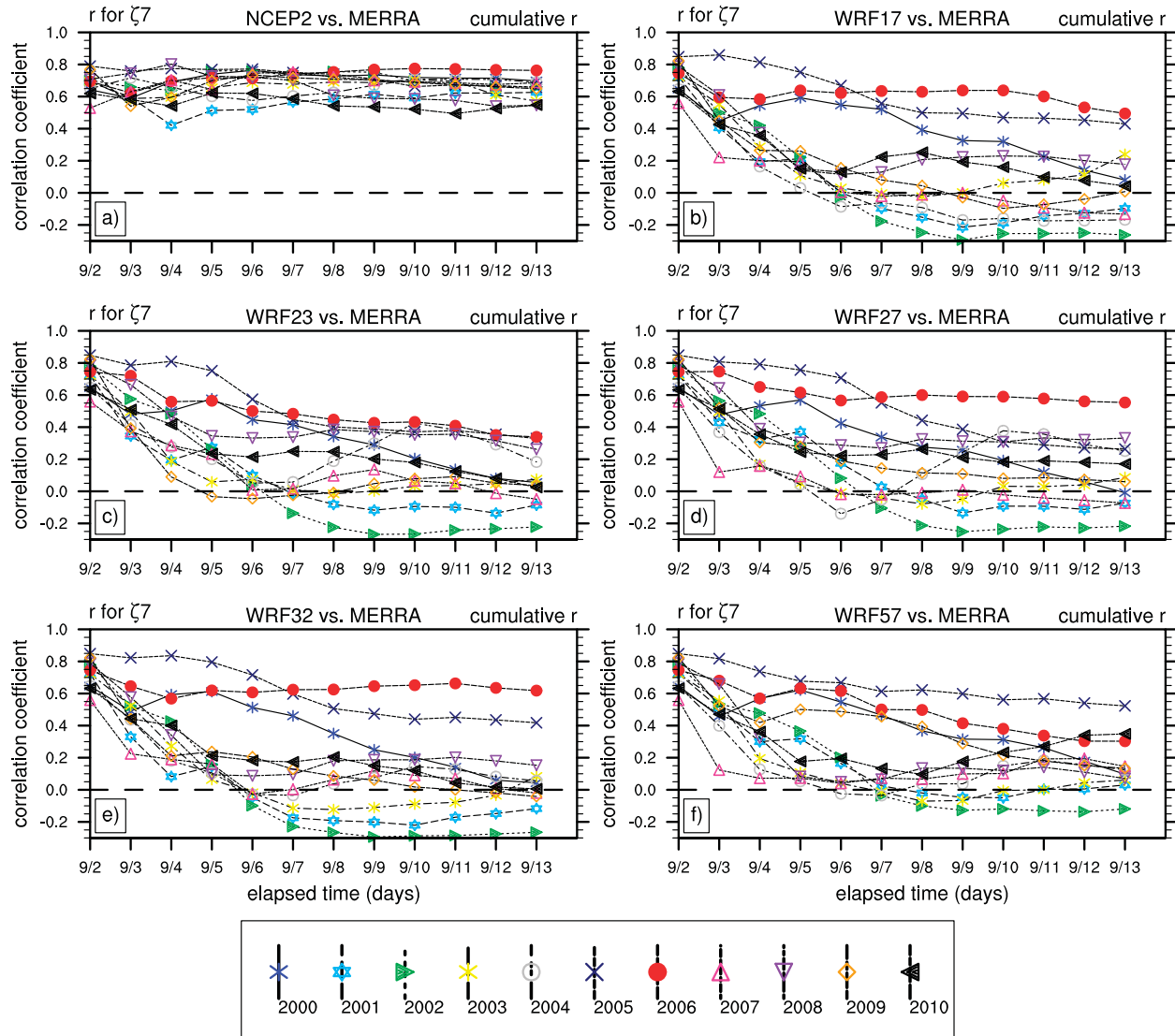
FIG. 9. An 11-yr comparison of correlations r vs elapsed time for modeled Hovmöller $\zeta 7$ distributions for the five selected WRF configurations from Fig. 6, vs MERRA for 2–13 Sep 2000–10 valid at 0000 UTC: (a) NCEP2, (b) WRF17, (c) WRF23, (d) WRF27, (e) WRF32, and (f) WRF57.

daily circulation patterns that include transient AEWs. Evaluation of concomitant precipitation simulations is reported in a forthcoming companion paper, although the dependence of precipitation variability on AEW behavior is noted. Some 64 WRF configurations are tried by using different combinations of available WRF parameterizations: CPS, LSM, RAD, and PBL physics. Simulated circulation data are compared to MERRA, which provides an independent estimate of actual conditions at a relatively high horizontal resolution (Δx, $\Delta y = 1.25°$).

An initial evaluation is made for simulations covering the period 2–13 September 2006. The mean 2–13 September zonal wind circulation for three of the better

performing configurations of WRF is compared to the reanalysis results. WRF produces a monsoon layer of westerlies in the lower troposphere, realistic negative wind shear with altitude, but a somewhat weakened AEJ core at 700 hPa, instead of the observed level of 600 hPa. Simulated near-surface monsoon westerlies are stronger than observed near the Gulf of Guinea coastline and the monsoon layer is consequently too thick, reaching to 700 hPa, instead being limited to a more reasonable ceiling of about 850 hPa.

Daily WRF 700-hPa circulation for select configurations is compared to MERRA, identifying vorticity centers and corresponding wave troughs. Allowing for better
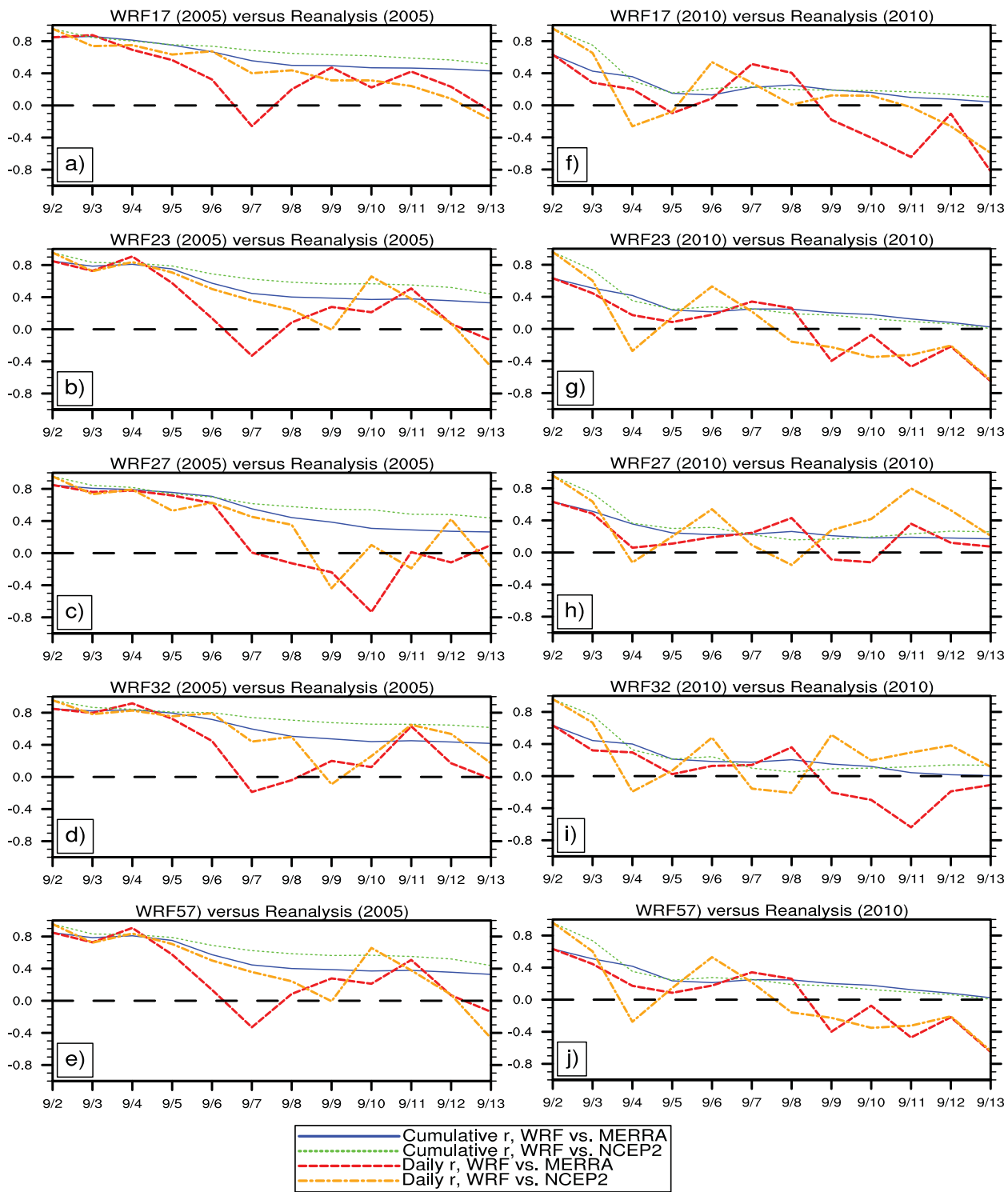
FIG. 10. As in Fig. 9, but for the cumulative r and daily modeled Hovmöller $\zeta 7$ distributions vs MERRA for 2–13 Sep (a)–(e) 2005 and (f)–(j) 2010.

spatial detail reflected in the higher-resolution WRF results, several prominent WRF AEWs that form during the 12-day simulation are identified with corresponding reanalysis features. The tracks of four WRF AEW vorticity maxima systems occurring during the study period (2–13 September) are compared with the reanalysis, showing small differences in path and 0000 UTC positions. At least two of the WRF AEWs move slower than their MERRA counterparts over land, but later catch up over the Atlantic. Lags in WRF AEW propagation speeds are undoubtedly related to the too weak core speed of the modeled AEJ, discussed above. There is evidence that WRF AEW tracks agree better with the relatively high-resolution MERRA reanalysis than with the coarser-resolution NCEP2, implying that the dynamic downscaling adds spatial detail to the analysis.

Objective validation scores are computed for comparisons between WRF and reanalysis Hovmöller time–longitude distributions of 0000 UTC 700-hPa vorticity, averaged between 5° and 20°N. These Hovmöller distributions show the westward tracks of the four AEWs and their intensities, appearing as diagonal swaths of relative vorticity maxima. Alternative parameterizations influence the simulation of AEW vorticity maxima and tracks, borne out by the range of validation scores for the 64 WRF configurations summarized on Taylor diagrams. The best WRF performers achieve vorticity correlations (against reanalysis) of between 0.40 and 0.60 and spatiotemporal variability amplitudes only slightly higher than in the reanalysis. A parallel simulation by the benchmark RM3 achieves a higher correlation against the reanalysis, but features reduced spatiotemporal variability amplitudes. The largest favorable impact on WRF vorticity simulation is realized by selecting the GD CPS. This preference may reflect the more versatile skill of that scheme's ensemble approach to computing the two-way interaction between convection and large-scale circulation (Grell 2002). Vorticity simulations using this scheme achieve higher correlations with reanalysis than the remaining simulations using the KF CPS (Kain 2004). The impacts of other model parameterizations are more ambiguous. More consistently favorable results are obtained using the Rt RAD scheme rather than the CM RAD. Configurations incorporating the MN PBL and the NO LSM did not perform well, but there are no unambiguous impacts attributed to using the remaining PBL and LSM schemes.

The reanalysis simulation for 2–13 September 2006 includes a large potential vorticity maximum at 700 hPa centered on 12°–13°N. Previous research (Hsieh and Cook 2008; Berry and Thorncroft 2005, 2012) indicates that AEWs can be triggered by intense convection, which reverses the meridional potential vorticity gradient, leads

to Charney–Stern instability, and contributes to baroclinic growth. Analysis of the 12-day mean potential vorticity at 700 hPa (not shown) for the WRF2, WRF27, WRF32, and WRF57 simulations shows discrepancies versus MERRA. For example, WRF2, which did not score well, simulates high mean potential vorticity (PV) too far north, implying deficiencies in where Charney–Stern instabilities create new AEWs and implying the AEW tracks that are too far north. Indeed, in 2006, WRF2 vorticity maxima are farther displaced from MERRA locations than more skillful simulations.

Examination of the cumulative and noncumulative daily r values versus elapsed time for selected WRF configurations for 2006 demonstrates some WRF skill in simulating vorticity centers up to 9 days.

Validation statistics for selected WRF configurations simulating the parallel period during 10 additional years indicate that results for 2006 are much more favorable than for other years. In fact, during most years, even the best WRF configurations fail to produce 700-hPa vorticity distributions with any correlation to reanalysis after a day or two.

The WRF simulations documented here for 2006 are less skillful in reproducing observed vorticity patterns than the benchmark RM3 simulation. Simulations for the same period during 10 additional years with selected WRF configurations are all less skillful than for 2006. This evaluation of simulated daily meteorological fields does not preclude the model producing realistic seasonal mean climate fields, especially if many of the high-frequency errors are random. While 64 model configurations cover a wide range of configurations, the testing reported here is not exhaustive. Results favor WRF27 (see Table 2) as the configuration achieving the best overall performance. This is sustained by the precipitation validation reported in a forthcoming companion paper, which describes the evaluation of WRF precipitation variability from the same 64 simulations. Future work should explore the performance of new parameterizations for simulating West African meteorology and climate.

from NASA's Global Hydrology Center website (http://airbornescience.nsstc.nasa.gov/namma), and NCEP Reanalysis-2 data were provided by the NOAA/ESRL/Physical Sciences Division, Boulder, Colorado, from their website (http://www.esrl.noaa.gov/psd).

REFERENCES

Benjamin, S. G., and Coauthors, 2004: An hourly assimilation–forecast cycle: The RUC. *Mon. Wea. Rev.,* **132,** 495–518, doi:10.1175/1520-0493(2004)132<0495:AHACTR>2.0.CO;2.

Berry, G. J., and C. Thorncroft, 2005: Case study of an intense African easterly wave. *Mon. Wea. Rev.,* **133,** 752–766, doi:10.1175/MWR2884.1.

——, and C. D. Thorncroft, 2012: African easterly wave dynamics in a mesoscale numerical model: The upscale role of convection. *J. Atmos. Sci.,* **69,** 1267–1283, doi:10.1175/JAS-D-11-099.1.

Bromwich, D. H., F. O. Otieno, K. M. Hines, K. W. Manning, and E. Shilo, 2013: Comprehensive evaluation of Polar Weather Research and Forecasting model performance in the Antarctic. *J. Geophys. Res.,* **118,** 274–292, doi:10.1029/2012JD018139.

Bukovsky, M. S., and D. J. Karoly, 2011: A regional modeling study of climate change impacts on warm-season precipitation in the central United States. *J. Climate,* **24,** 1985–2002, doi:10.1175/2010JCLI3447.1.

Burpee, R. W., 1972: The origin and structure of easterly waves in the lower troposphere of North Africa. *J. Atmos. Sci.,* **29,** 77–90, doi:10.1175/1520-0469(1972)029<0077:TOASOE>2.0.CO;2.

Cassano, J. J., M. E. Higgins, and M. W. Seefeldt, 2011: Performance of the Weather Research and Forecasting model for month-long pan-Arctic simulations. *Mon. Wea. Rev.,* **139,** 3469–3488, doi:10.1175/MWR-D-10-05065.1.

Chen, F., and J. Dudhia, 2001: Coupling an advanced land surface–hydrology model with the Penn State–NCAR MM5 Modeling System. Part II: Preliminary model validation. *Mon. Wea. Rev.,* **129,** 587–604, doi:10.1175/1520-0493(2001)129<0587:CAALSH>2.0.CO;2.

Chiao, S., and G. S. Jenkins, 2010: Numerical investigations on the formation of Tropical Storm Debby during NAMMA-06. *Wea. Forecasting,* **25,** 866–884, doi:10.1175/2010WAF2222313.1.

Collins, W. D., and Coauthors, 2004: Description of the NCAR Community Atmosphere Model (CAM 3.0). NCAR Tech. Note NCAR/TN–464+STR, 214 pp.

Cook, K. H., 1999: Generation of the African easterly jet and its role in determining West African precipitation. *J. Climate,* **12,** 1165–1184, doi:10.1175/1520-0442(1999)012<1165:GOTAEJ>2.0.CO;2.

Crétat, J., B. Pohl, Y. Richard, and P. Drobinski, 2012: Uncertainties in simulating regional climate of southern Africa: Sensitivity to physical parameterizations using WRF. *Climate Dyn.,* **38,** 613–634, doi:10.1007/s00382-011-1055-8.

Delonge, R., cited 2013: NAMMA Kawsara Senegal Radiosondes: 15 August to 16 September 2006. NASA Global Hydrology Resource Center. [Available online at http://ghrc.nsstc.nasa.gov/hydro/details.pl?ds=namsenegal.]

Diedhiou, A., S. Janicot, A. Viltard, P. de Felice, and H. Laurent, 1999: Easterly wave regimes and associated convection over West Africa and tropical Atlantic: Results from the NCEP/NCAR and ECMWF reanalyses. *Climate Dyn.,* **15,** 795–822, doi:10.1007/s003820050316.

Done, J., C. A. Davis, and M. Weisman, 2004: The next generation of NWP: Explicit forecasts of convection using the Weather Research and Forecasting (WRF) model. *Sci. Lett.,* **5,** 110–117, doi:10.1002/asl.72.

Druyan, L. M., M. Fulakeza, and P. Lonergan, 2006: Mesoscale analyses of West African summer climate: Focus on wave disturbances. *Climate Dyn.,* **27,** 459–481, doi:10.1007/s00382-006-0141-9.

——, ——, ——, and E. Noble, 2009: Regional climate model simulation of the AMMA Special Observing Period #3 and the pre-Helene easterly wave. *Meteor. Atmos. Phys.,* **105,** 191–210, doi:10.1007/s00703-009-0044-5.

——, and Coauthors, 2010: The WAMME regional model intercomparison study. *Climate Dyn.,* **35,** 175–192, doi:10.1007/s00382-009-0676-7.

Flaounas, E., S. Bastin, and S. Janicot, 2011: Regional climate modelling of the 2006 West African monsoon: Sensitivity to convection and planetary boundary layer parameterisation using WRF. *Climate Dyn.,* **36,** 1083–1105, doi:10.1007/s00382-010-0785-3.

——, S. Janicot, S. Bastin, and R. Roca, 2012: The West African monsoon onset in 2006: Sensitivity to surface albedo, orography, SST and synoptic scale dry-air intrusions using WRF. *Climate Dyn.,* **38,** 685–708, doi:10.1007/s00382-011-1255-2.

Franklin, J. L., and D. P. Brown, 2008: Atlantic hurricane season of 2006. *Mon. Wea. Rev.,* **136,** 1174–1200, doi:10.1175/2007mwr2377.1.

Giorgi, F., 1990: Simulation of regional climate using a limited area model nested in a general circulation model. *J. Climate,* **3,** 941–963, doi:10.1175/1520-0442(1990)003<0941:SORCUA>2.0.CO;2.

——, and L. O. Mearns, 1991: Approaches to the simulation of regional climate change: A review. *Rev. Geophys.,* **29,** 191–216, doi:10.1029/90RG02636.

Grell, G. A., 2002: A generalized approach to parameterizing convection combining ensemble and data assimilation techniques. *Geophys. Res. Lett.,* **29,** 1693, doi:10.1029/2002GL015311.

Hagos, S. M., and K. H. Cook, 2007: Dynamics of the West African monsoon jump. *J. Climate,* **20,** 5264–5284, doi:10.1175/2007JCLI1533.1.

Harrold, M., 2012: The Developmental Testbed Center's final report on the inter-comparison of the WRFv3.3.1 AFWA operational and RRTMG-Replacement configurations. Developmental Testbed Center, Boulder, CO, 40 pp.

Heikkilä, U., A. Sandvik, and A. Sorteberg, 2010: Dynamical downscaling of ERA-40 in complex terrain using the WRF regional climate model. *Climate Dyn.,* **37,** 1551–1564, doi:10.1007/s00382-010-0928-6.

Hodges, K. I., 1995: Feature tracking on the unit sphere. *Mon. Wea. Rev.,* **123,** 3458–3465, doi:10.1175/1520-0493(1995)123<3458:FTOTUS>2.0.CO;2.

Hong, S.-Y., J. Dudhia, and S.-H. Chen, 2004: A revised approach to ice microphysical processes for the bulk parameterization of clouds and precipitation. *Mon. Wea. Rev.,* **132,** 103–120, doi:10.1175/1520-0493(2004)132<0103:ARATIM>2.0.CO;2.

——, Y. Noh, and J. Dudhia, 2006: A new vertical diffusion package with an explicit treatment of entrainment processes. *Mon. Wea. Rev.,* **134,** 2318–2341, doi:10.1175/MWR3199.1.

Hovmöller, E., 1949: The trough-and-ridge diagram. *Tellus,* **1,** 62–66, doi:10.1111/j.2153-3490.1949.tb01260.x.

Hsieh, J.-S., and K. H. Cook, 2008: On the instability of the African easterly jet and the generation of African waves: Reversals of the potential vorticity gradient. *J. Atmos. Sci.,* **65,** 2130–2151, doi:10.1175/2007JAS2552.1.

Iacono, M. J., J. S. Delamere, E. J. Mlawer, M. W. Shephard, S. A. Clough, and W. D. Collins, 2008: Radiative forcing by long-lived greenhouse gases: Calculations with the AER radiative

transfer models. *J. Geophys. Res.,* **113,** D13103, doi:10.1029/2008JD009944.

Janjić, Z., 2002: Nonsingular implementation of the Mellor–Yamada level 2.5 scheme in the NCEP Meso model. NCEP Office Note 437, 61 pp.

Kain, J. S., 2004: The Kain–Fritsch convective parameterization: An update. *J. Appl. Meteor.,* **43,** 170–181, doi:10.1175/1520-0450(2004)043<0170:TKCPAU>2.0.CO;2.

Kanamitsu, M., W. Ebisuzaki, J. Woollen, S.-K. Yang, J. J. Hnilo, M. Fiorino, and G. L. Potter, 2002: NCEP–DOE AMIP-II Reanalysis (R-2). *Bull. Amer. Meteor. Soc.,* **83,** 1631–1643, doi:10.1175/BAMS-83-11-1631.

Lebel, T., A. Diedhiou, and H. Laurent, 2003: Seasonal cycle and interannual variability of the Sahelian rainfall at hydrological scales. *J. Geophys. Res.,* **108,** 8389, doi:10.1029/2001JD001580.

Leung, L. R., and Y. Qian, 2009: Atmospheric rivers induced heavy precipitation and flooding in the western U.S. simulated by the WRF regional climate model. *Geophys. Res. Lett.,* **36,** L03820, doi:10.1029/2008GL036445.

Liang, X.-Z., K. E. Kunkel, and A. N. Samel, 2001: Development of a regional climate model for U.S. Midwest applications. Part I: Sensitivity to buffer zone treatment. *J. Climate,* **14,** 4363–4378, doi:10.1175/1520-0442(2001)014<4363:DOARCM>2.0.CO;2.

Lim, J.-O. J., and S.-Y. Hong, 2005: Effects of bulk ice microphysics on the simulated monsoonal precipitation over East Asia. *J. Geophys. Res.,* **110,** D24201, doi:10.1029/2005JD006166.

Lynn, B. H., R. Healy, and L. M. Druyan, 2009: Quantifying the sensitivity of simulated climate change to model configuration. *Climatic Change,* **92,** 275–298, doi:10.1007/s10584-008-9494-x.

Martius, O., C. Schwierz, and H. C. Davies, 2006: A refined Hovmöller diagram. *Tellus,* **58A,** 221–226, doi:10.1111/j.1600-0870.2006.00172.x.

Nakanishi, M., and H. Niino, 2006: An Improved Mellor–Yamada level-3 model: Its numerical stability and application to a regional prediction of advection fog. *Bound.-Layer Meteor.,* **119,** 397–407, doi:10.1007/s10546-005-9030-8.

Patricola, C. M., and K. H. Cook, 2010: Northern African climate at the end of the twenty-first century: An integrated application of regional and global climate models. *Climate Dyn.,* **35,** 193–212, doi:10.1007/s00382-009-0623-7.

Pleim, J. E., 2007: A combined local and nonlocal closure model for the atmospheric boundary layer. Part II: Application and evaluation in a mesoscale meteorological model. *J. Appl. Meteor. Climatol.,* **46,** 1396–1409, doi:10.1175/JAM2534.1.

——, and A. Xiu, 2003: Development of a land surface model. Part II: Data assimilation. *J. Appl. Meteor.,* **42,** 1811–1822, doi:10.1175/1520-0450(2003)042<1811:DOALSM>2.0.CO;2.

Pohl, B., J. Crétat, and P. Camberlin, 2011: Testing WRF capability in simulating the atmospheric water cycle over equatorial East Africa. *Climate Dyn.,* **37,** 1357–1379, doi:10.1007/s00382-011-1024-2.

Redelsperger, J.-L., C. D. Thorncroft, A. Diedhiou, T. Lebel, D. J. Parker, and J. Polcher, 2006: African Monsoon Multidisciplinary Analysis: An international research project and field campaign. *Bull. Amer. Meteor. Soc.,* **87,** 1739–1746, doi:10.1175/BAMS-87-12-1739.

Reed, R. J., E. Klinker, and A. Hollingsworth, 1988: The structure and characteristics of African easterly wave disturbances as determined from the ECMWF operational analysis/forecast system. *Meteor. Atmos. Phys.,* **38,** 22–33, doi:10.1007/BF01029944.

Rienecker, M. M., and Coauthors, 2011: MERRA: NASA's Modern-Era Retrospective Analysis for Research and Applications. *J. Climate,* **24,** 3624–3648, doi:10.1175/JCLI-D-11-00015.1.

Schmidlin, F., cited 2013: NAMMA Praia Cape Verde Radiosonde: 19 August to 14 September 2006. NASA Global Hydrology Resource Center. [Available online at http://ghrc.nsstc.nasa.gov/hydro/details.pl?ds=namradio.]

Skamarock, W. C., and Coauthors, 2008: A description of the Advanced Research WRF version 3. NCAR Tech. Note NCAR/TN–4751STR, 113 pp.

Sultan, B., and S. Janicot, 2000: Abrupt shift of the ITCZ over West Africa and intra-seasonal variability. *Geophys. Res. Lett.,* **27,** 3353–3356, doi:10.1029/1999GL011285.

Taylor, C. M., 2008: Intraseasonal land–atmosphere coupling in the West African monsoon. *J. Climate,* **21,** 6636–6648, doi:10.1175/2008JCLI2475.1.

Taylor, K. E., 2001: Summarizing multiple aspects of model performance in a single diagram. *J. Geophys. Res.,* **106,** 7183–7192, doi:10.1029/2000JD900719.

Thorncroft, C., and K. Hodges, 2001: African easterly wave variability and its relationship to Atlantic tropical cyclone activity. *J. Climate,* **14,** 1166–1179, doi:10.1175/1520-0442(2001)014<1166:AEWVAI>2.0.CO;2.

Vizy, E. K., and K. H. Cook, 2009: Tropical storm development from African easterly waves in the eastern Atlantic: A comparison of two successive waves using a regional model as part of NASA AMMA 2006. *J. Atmos. Sci.,* **66,** 3313–3334, doi:10.1175/2009JAS3064.1.

Zipser, E. J., and Coauthors, 2009: The Saharan air layer and the fate of African easterly waves—NASA's AMMA field study of tropical cyclogenesis. *Bull. Amer. Meteor. Soc.,* **90,** 1137–1156, doi:10.1175/2009BAMS2728.1.